

Ultra-high Tunneling Electroresistance Ratio (2×10^4) & Endurance (10^8) in Oxide Semiconductor-Hafnia Self-rectifying (1.5×10^3) Ferroelectric Tunnel Junction

Junghyeon Hwang¹, Chaeheon Kim¹, Hunbeom Shin¹, Hwayoung Kim², Sang-Hee Ko Park² and Sanghun Jeon¹

¹School of Electrical Engineering, Korea Advanced Institute of Science and Technology (KAIST), Korea, ²Department of Materials Science and Engineering, Korea Advanced Institute of Science and Technology (KAIST)

Email: jeonsh@kaist.ac.kr

Abstract: In this study, we present a remarkable improvement in the performance of hafnia-based ferroelectric tunnel junctions (FTJs) using oxygen scavenging technology and extremely low-damage (ELD) deposition, leading to a significant increase in the tunneling electroresistance ratio (TER) ($>2 \times 10^4$), on-current density ($>10^{-2} \text{ A/cm}^2$), and self-rectifying ratio (RR) ($>1.5 \times 10^3$). First-principles DFT simulations were also used to evaluate how the asymmetric oxygen vacancy (V_O) distribution affected FTJs. As an array-level demonstration of the proposed approach, we experimentally built an FTJ-based XNOR synapse array and verified its operation for binary neural networks (BNN).

Introduction: A number of significant advantages of the FTJ over conventional technologies have been demonstrated, including their capacity for non-destructive read operations, low power consumption, and fast switching operation. Despite having a lot of merits, FTJs still have some device issues that need to be resolved in order to reach their full potentials, such as low TER values and low on-current levels [1-6]. In this study, we have made an impressive improvement in TER (2×10^4) and significantly increased on-current density (Fig. 1). ELD deposition process allows us to reduce the disorder in the HZO thin film, producing high ferroelectricity even at relatively thin thickness. By deliberately increasing V_O at one interface, oxygen scavenging technology enhances the asymmetry of FTJ. (Fig. 2) Furthermore, we have examined the effect using first-principles computations. In addition, we built an FTJ-based XNOR synapse array for BNN to provide its array-level demonstration of our suggested approach.

The Validation of Working Principles by DFT Calculation: To understand the effect of asymmetric V_O distribution on FTJ, we performed first-principles DFT calculations utilizing the nonequilibrium Green's function and coherent potential approximation method (NECPA-DFT) with NANODSIM [7]. To validate our approach, we compared the band structures of TiN, HfO₂, and In₂O₃ obtained from our calculations with those simulated using the VASP and found a good agreement (Fig. 3 (a)-(c)). Fig. 3(d) shows DFT calculation results of the potential barrier for the TiN/In₂O₃/HfO₂/TiN structure FTJ as a function of V_O concentration in the In₂O₃ for different polarization directions. It is clear that the barrier falls as the V_O concentration rises only when the polarization points to the right.

Experimental Verification: Fig. 4(a)-(b) present X-ray spectroscopy data (EDS) and high-resolution transmission electron microscopy (HR-TEM) images of the FTJ, respectively. Fig. 4(c) illustrates the key-process flow for the fabrication of FTJ. The process begins with the deposition and patterning of the bottom electrode (BE) on the SiO₂/Si substrate, followed by the deposition of the HZO layer. Then, TiN as a sacrificial layer is performed and followed by PMA 600°C for 10 seconds. The sacrificial layer is then etched, and InO and top electrode (TE) are deposited and patterned. When utilizing ELD deposition, Fig. 5(a) shows the P-E curve of a

ferroelectric capacitor with enhanced ferroelectricity compared to the conventional process. Fig. 5(b) illustrates the $2P_r$ values of ferroelectric capacitors at various ELD plasma powers and thicknesses. Even with 4.5 nm thick HZO, we still managed to reach a high $2P_r$ value of $44 \mu\text{C/cm}^2$. Geometric phase analysis (GPA) data in Fig. 6 demonstrate that, when the ELD process is applied, disorders are reduced in comparison to the conventional process. Fig. 7(a)-(b) depicts the XPS depth spectra at the top interface of In 3d and Hf 4f. Fig. 7(b) illustrates the relative area fractions of suboxides with the depth in InO and HZO, for various thicknesses of InO. The presence of InO at the interface provides oxygen to HfO₂ and remaining V_O s in the InO layer. Fig. 8 illustrates the on and off-current trends of the FTJ with the thickness of InO, in agreement with the findings presented in Fig. 7. Fig. 9 presents the I-V curve of the TiN/InO/HZO/TiN stack FTJ with strong and weak ferroelectricity.

Demonstration of BNN using FTJ Array: Fig. 10 presents the imprinted P-E curve of the TiN/InO/HZO/TaN stack FTJ showing self-rectifying characteristics. Fig. 11 exhibits the I-V curve of the FTJ, demonstrating a high RR of 1.5×10^3 , a high TER ($>2 \times 10^4$), and a high on-current ($>10^{-2} \text{ A/cm}^2$). Fig. 12 illustrates the TER and RR values as a function of the read voltage, while Fig. 13 presents the TER and RR values with the HZO ratio. Fig. 14 shows the endurance characteristics of the FTJ, with a clear distinction between the two states even after 10^8 cycles. To evaluate its suitability for array-scale applications, we fabricated 12×12 arrays of FTJs on a 4-inch wafer (Fig. 15(a)). Fig. 15(b) depicts the XNOR operation method for a BNN utilizing 2-FTJ synapses. The measured weight map with the 12×12 array of FTJs of a specific region within the BNN is presented in Fig. 15(c), and the resulting XNOR and accumulation (XAC) values, as calculated by the input pattern, are displayed in Fig. 15(d). Fig. 16 presents excellent device-to-device variation among 100 FTJs measured in a cross-point array structure. The measurement setup for the array of FTJs is displayed in Fig. 17. We constructed a BNN using the FTJ cross-point array to simulate the CIFAR-10 dataset by using experimentally measured electrical and variation data (Fig. 18).

Conclusion: We have achieved exceptional performance in hafnia-based FTJ by utilizing ELD deposition and oxygen-scavenging technology. Furthermore, our results were supported by first-principles calculations simulated by NECPA-DFT. We fabricated an FTJ with self-rectifying characteristics as a cross-point array using a TaN bottom electrode, successfully demonstrating XAC operation for BNN.

Acknowledgment This work was supported by Grant Nos. NRF-2020M3F3A2A02082450 and NRF-2020M3F3A2A01081916.

References [1] Y. Goh et al., *IEDM* 2021, pp.378 [2] M. Hoffmann et al., *APL* 2022, 120, 122901, 2022 [3] F. Liu et al., *IEEE EDL*, 42, 696, 2021, [4] K.-Y. Hsiang et al., *IEEE EDL*, 42, 1464, 2021 [5] K.-K. Min et al., *Appl. Surf. Sci.*, 573, 151566, 2022 [6] R. Athle et al., *ACS AEM*, 4, 1002, 2022 [7] Y. Zhu et al., *Phys. Rev. B*, 88, 205415, 2013

Motivation

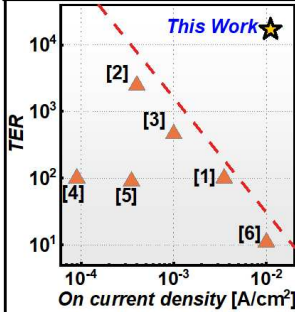


Fig. 1. Benchmark of our FTJ. This work shows the record-high TER and high current density.

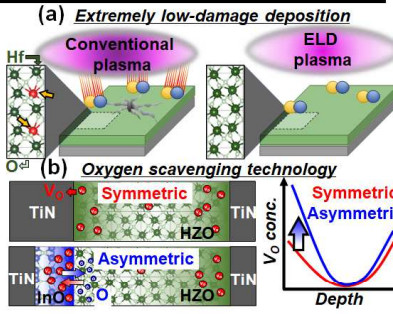


Fig. 2. Strategy to enhance TER and on-current in FTJ by (a) extremely low-damage (ELD) deposition and (b) oxygen scavenging technology.

Working Principles with First-principles Calculations

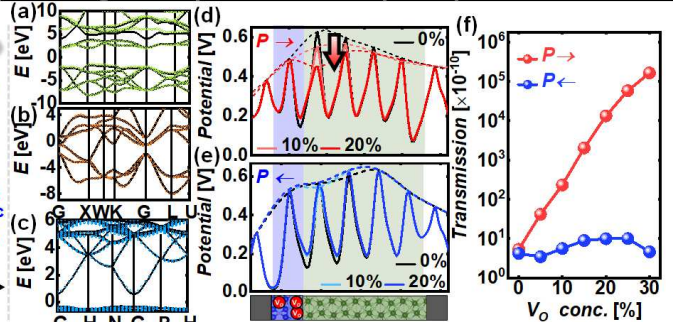


Fig. 3. Band structures of (a) HfO_2 (b) TiN and (c) In_2O_3 obtained by VASP (solid) and NANODSIM (dot). Potential profiles at (d) P^- and (e) P^- (f) Transmission coefficient with V_0 concentration.

Experimental Verification of High-performance FTJ using Oxygen Scavenging Technology

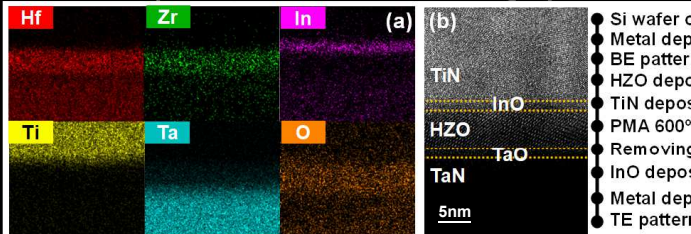


Fig. 4. (a) EDS in STEM images of Hf, Zr, In, Ti, Ta, and O (b) HR-TEM image of $\text{TiN}/\text{InO}/\text{HZO}/\text{TaN}$ stack FTJ. (c) Key process flow of the FTJ devices and cross-point array

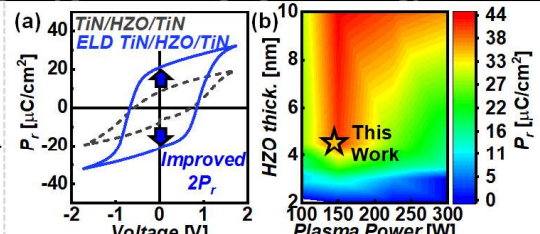


Fig. 5. (a) P-E curves of MFM using ELD (b) Color map of P_r with various HZO thickness and ELD plasma power.

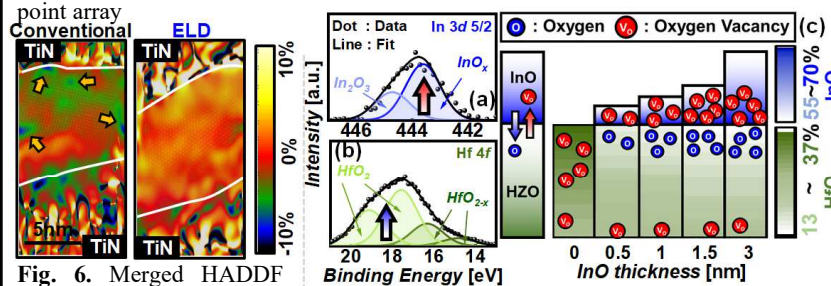


Fig. 6. Merged HADDF STEM and GPA results for MFM with the conventional process and ELD process.

Fig. 7. XPS depths spectra of (a) $\text{In } 3d$ and (b) $\text{Hf } 4f$ in a top interface for FTJ (c) The relative areal fraction of suboxide along the depth in InO and HZO with various InO thickness.

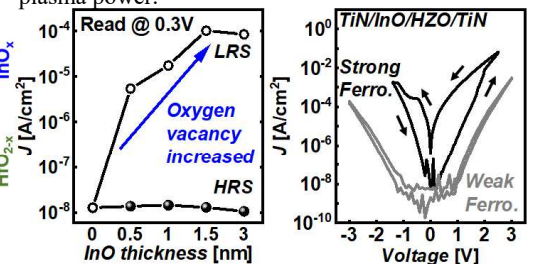


Fig. 8. On & off current density of FTJ with various InO thickness. Fig. 9. DC-IV of FTJ with strong ferro. and weak ferro.

Self-rectifying & High-performance FTJ with V_0 Engineering and its Array Level Demonstration

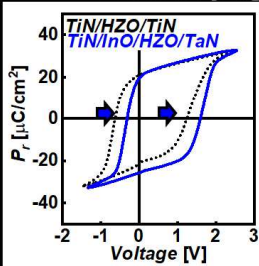


Fig. 10. Imprinted P-V hysteresis curve of $\text{TiN}/\text{InO}/\text{HZO}/\text{TaN}$ FTJ

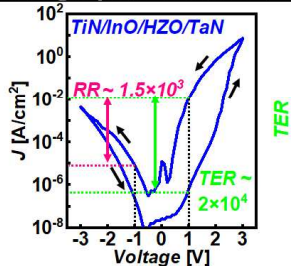


Fig. 11. Representative DC-IV of $\text{TiN}/\text{InO}/\text{HZO}/\text{TaN}$ FTJ showing record high TER

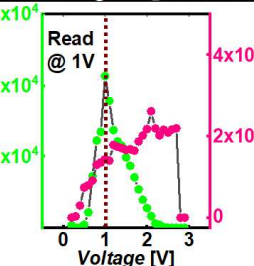


Fig. 12. TER & RR with read voltage

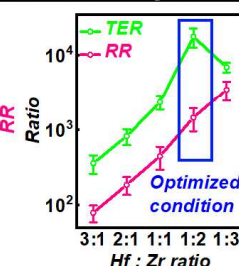


Fig. 13. TER and RR of FTJ with $\text{Hf} : \text{Zr}$ ratio

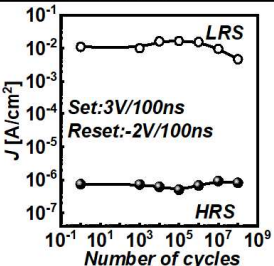


Fig. 14. Endurance characteristics of FTJ

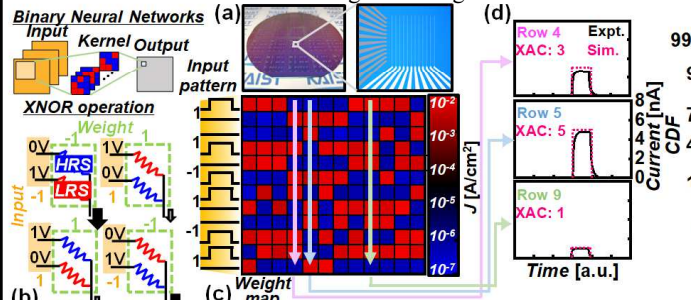


Fig. 15. (a) Fabricated 4-inch wafer with 12×12 FTJ array (b) XNOR operation in 2-FTJ based synapse. (c) Measured 12×12 BNN weight map (d) Measured XNOR and accumulation value in the selected row.

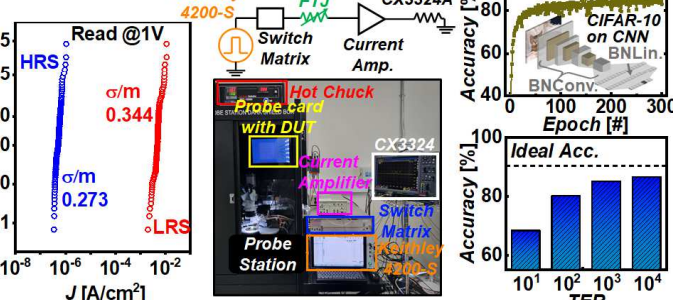


Fig. 16. D to D variation of 100 devices in FTJ array

Fig. 17. Schematic and photo of the FTJ array measurement setup

Fig. 18. BNN simulation with increasing TER